Applied Surface Science 462 (2018) 226–236

Contents lists available at ScienceDirect

Applied Surface Science

journal homepage: www.elsevier.com/locate/apsusc

Full Length Article

Study of iron oxide magnetic nanoparticles obtained via pulsed laser ablation of iron in air

Valery A. Svetlichnyi[a], Anastasiia V. Shabalina[a,*], Ivan N. Lapin[a], Darya A. Goncharova[a], Dmitry A. Velikanov[b], Aleksey E. Sokolov[b]

[a] Siberian Physical-Technical Institute of Tomsk State University, Novosobornaya sq., 1, Tomsk 634050, Russia
[b] Kirensky Institute of Physics, Federal Research Center KSC SB RAS, Akademgorodok 50, bld. 38, Krasnoyarsk 660036, Russia

ARTICLE INFO

Keywords:
Pulsed laser ablation in air
Iron oxide
Nanostructures
Magnetic properties
Thermal transformation

ABSTRACT

Magnetic nanoparticles were obtained using the nanosecond pulsed laser ablation (Nd:YAG laser, 1064 nm, 7 ns) of an iron target in air at atmospheric pressure. The particles obtained were further annealed at four different temperatures. The composition, structure and properties of all obtained powders were investigated using X-ray diffraction (XRD), DSC, attenuated total reflection Fourier-transform infrared spectroscopy (ATR-FTIR), Raman spectroscopy, TEM, SAED and other techniques. The initial sample was found to contain monoclinic magnetite and iron nitrides. Presumably, magnetite presents in the form of spherical particles with the distribution maximum of 12–15 nm, and nitrides take the form of lamellas and rolls. Thermal treatment of the sample led to particle enlargement and phase transformations, first, to cubic magnetite, then to a Fe_3O_4, α-Fe_2O_3 and γ-Fe_2O_3 mixture, and finally to the pure hematite phase. Zeta-potential, BET surface area and magnetic properties changed with the annealing as well. The obtained materials exhibited different properties that make them in demand in different fields, from biomedicine to technology.

1. Introduction

Pulsed laser ablation (PLA) is a suitable method for obtaining of the "pure nanoparticles" of various materials without use or with a minimal amount of chemical precursors [1]. Currently, the most widespread method of PLA is performed in a liquid, which allows nanoparticles (NPs) to be obtained straightly in the form of colloids [2]. The greatest progress in understanding the ablation mechanisms has been achieved in the PLA of noble metal NPs [3,4] and in the synthesis of a number of oxides obtained by the PLA of targets made of reactive materials [5,6]. However, the production of composite nanomaterials and NPs in the form of powders is often required for many applications. For example, it is required for catalysis [7] or for subsequent modification of the particles; for their additional treatment or for re-dispersion in other liquids with special properties. In this case, using PLA in liquids makes the powder-obtaining process quite complicated. It requires the additional stages of concentrating and drying the dispersions, which not only complicates the production procedure but can affect the composition and structure of the particles produced. An ablation in gaseous media [8] can be an alternative to PLA in liquid in some cases. It is especially attractive, for example, for the obtainment of oxide NPs. Moreover, the changing of the gas mixture's composition and its pressure makes it possible to control the oxidation processes quite efficiently [9]. Additional advantages and improved ablation efficiency can also be achieved at the PLA of magnetic materials using permanent magnets to accelerate the process of depositing the aerosol of magnetic particles onto the reactor walls.

Among the most interesting and promising magnetic NPs, iron oxides have been attracting the attention of scientists and engineers for decades. Magnetite, maghemite, hematite and other compounds of the Fe-O system in the nano state exhibit unique magnetic properties, allowing them to be used in such field as biomedicine (drug delivery [10], hyperthermia [11], etc.), energy storage and absorption of radiation [12], SERS analysis [13], agricultural applications [14], etc. Our research group has already obtained pure magnetite NPs via PLA in water [15]. The aim of this work was to obtain and characterize ultra-dispersed nanopowders using a nanosecond PLA of an iron target in air and studying the effect of the subsequent heat treatment on their composition, structure and functional (including magnetic) properties.

* Corresponding author.
E-mail address: shabalinaav@gmail.com (A.V. Shabalina).

https://doi.org/10.1016/j.apsusc.2018.08.116
Received 26 June 2018; Received in revised form 3 August 2018; Accepted 14 August 2018
Available online 15 August 2018
0169-4332/

2. Experimental

2.1. Synthesis of the materials

NPs were obtained using the focused radiation of an Nd:YAG laser LS-2131M-20 (LOTIS TII, Belarus). The PLA was carried out at the wavelength of 1064 nm. The pulse duration was 7 ns and the repetition frequency was maintained at 20 Hz. In this work, the total energy of the laser pulse from the nanosecond laser (150 mJ) was used. Changing the focusing allows one to change the pulse density of the radiation power (energy) on the target surface. In this case, a power density of 400 MW/cm^2 was chosen. This power density was optimal for the maximum yield under these experimental conditions (atmosphere, reactor size, total energy and the pulse duration).

An iron target (99.5%) of 40 × 40 × 5 mm was fixed in a lid on the back end of a cylindrical quartz glass reactor. The reactor was 200 mm in length, its internal diameter was 60 mm and the volume was ~565 cm^2. The front end of the reactor was closed with a polyethylene membrane, which was transparent for radiation. The laser beam was focused on the target surface by a long-focus (F = 500 mm) collecting lens. The initial radiation power density on the target surface was 400 MW/cm^2, as it was mentioned above. For the purpose of uniform irradiation of the target surface, it was automatically moved in the X–Y plane orthogonal to the laser beam.

The gas-plasma cloud formed as a result of ablation of the target and interacted with the air molecules. The NPs obtained settled on the reactor walls, forming a layer of a brown powder. To accelerate the NP deposition process and reduce the interaction of the laser beam with the NPs in the air, a belt of magnets was fixed around on the outside wall of the reactor. The ablation took 5 h. The powder was then mechanically removed from the walls. The average yield of NPs at the experiment parameters described was ~15 mg/h. The synthesis procedure was repeated several times to obtain a sufficient amount of the powder for the study. The same target and the radiation power density were used for the repeated experiments. The atmosphere was renewed naturally during the powder extraction from the reactor in the pauses of the PLA process.

The obtained sample was annealed in a muffle furnace SNOL 6.7/1300 (Lithuania) in the temperature range of 200–500 °C. The heating rate was 10 °C/min, and the holding time at a given temperature was 4 h. Next, the initial sample was marked as Fe_init. The Fe_T was used to mark the samples after annealing, where T is the annealing temperature. The Fe_Ar O_2 designation was used for the sample obtained by PLA in an argon medium supplemented with 20% oxygen (partial pressure).

2.2. Characterization of the materials

XRD patterns were obtained using XRD 6000 (Shimadzu, Japan). Phase composition was established using Powder Cell 2.4 (Germany) and PDF-4 database. ATR-FTIR spectra were obtained on the TENZOR 27 (Bruker, Germany) spectrometer. Raman spectra were recorded on a Raman microscope InVia (Renishaw, UK) at an excitation by a semiconductor laser with the maximal power of 100 mW, a wavelength of 785 nm and 50× objective. So as not to damage the samples with radiation, the spectra were recorded at the low power (0.5%), and the power density at the sample surface was 1.25 kW/cm^2.

Differential scanning calorimetry (DSC) and thermal gravimetric analysis (TGA) data were obtained using DSC 204 F1 Phoenix (Netzsch, Germany). A total of 4.1 mg of a sample was placed into the Al closed pan and heated from room temperature up to 600 °C with the rate of 10 °C/min. The sample was compacted in air, and the measurements were carried out in Ar flow (50 and 100 ml/min) without preliminary degassing. The air thus presented in the system.

The microstructure of the materials obtained was studied using transmission electron microscopy (TEM) on a Hitachi TEM System (Hitachi, Japan) on carbon-coated copper grids at 110 kV. Energy-dispersive X-ray analysis (EDX) was carried out at the system with electron and focused ion beams Quanta 200 3D (FEI Company, USA). The BET surface area of the powders was measured on a gas-adsorption analyzer of a specific surface and porosity TriStar II 3020 (Micromeritics, USA). Before analysis, the powder samples of the material were degassed in a vacuum (10^{-2} Torr) at 200 °C for 2 h. The zeta potential of the samples was measured on Omni S/N (Brookhaven, USA) in ZetaPALS mode with a BI-ZTU autotitrator (Brookhaven, USA) to change the pH; the previously described method was used [16]. The pH was adjusted using diluted solutions of KOH and HNO_3 (10^{-1} to 10^{-3} M). The solution of 10^{-2} M KNO_3 was used as a background electrolyte to maintain the ionic concentration. An average value from three measurements was used.

The magnetic properties of the materials were studied at room temperature using a vibrating sample magnetometer in a magnetic field of up to ± 20 kOe. Mechanical vibrations of the sample were provided by a vibrator of the original design [17]. The oscillation amplitude relative instability was 10^{-4} with a frequency of 10^{-5}. The system of four pickup coils was used for to register the signal. The dynamic range of the device was 5 × 10^{-6}–100 emu. For the magnetic measurements, the investigated samples were ground with KBr powder and pressed into the tablets.

3. Results and discussion

3.1. XRD study of the materials

XRD of the samples obtained by PLA in air and with subsequent thermal treatment, along with the sample ablated in Ar/O_2 mixture, are presented in Fig. 1. Three first patterns from the bottom are quite alike. They did not exhibit hematite peaks, but it is almost impossible to distinguish whether maghemite or magnetite is present in these three samples. Starting with the Fe_300 sample, hematite peaks appeared, and Fe_500 only contained this iron oxide phase. It is assumed that the Fe_300 and Fe_400 samples contained a mixture of all three phases. To establish the precise phase composition of the samples, other methods were applied.

3.2. DSC study of the materials

DSC data for the samples are presented in Fig. 2. Water loss was observed before 100 °C (the first endothermic peak). The Fe_500 sample

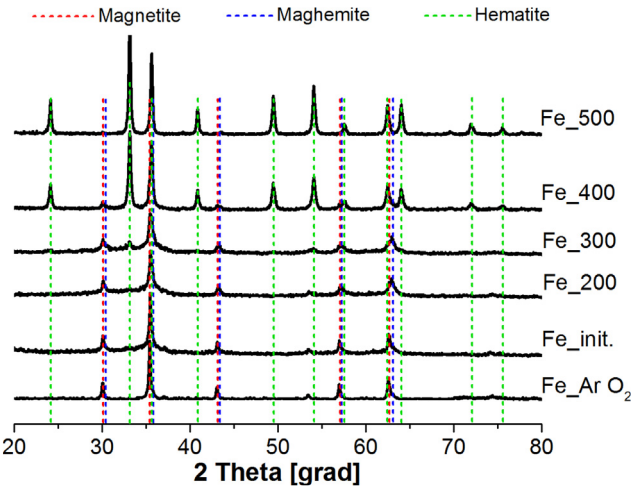

Fig. 1. X-ray diffraction patterns of the samples. Red for magnetite (PDF Card#04-015-3100); blue for maghemite (PDF Card#00-039-1346); green for hematite (PDF Card#01-089-0598). (For interpretation of the references to colour in this figure legend, the reader is referred to the web version of this article.)

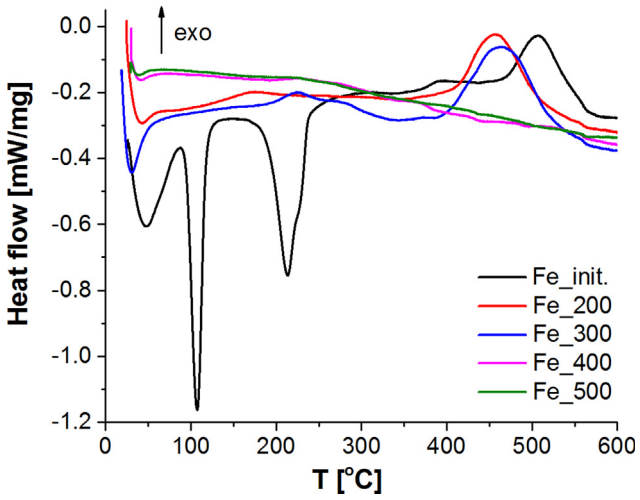

Fig. 2. DSC data for the samples.

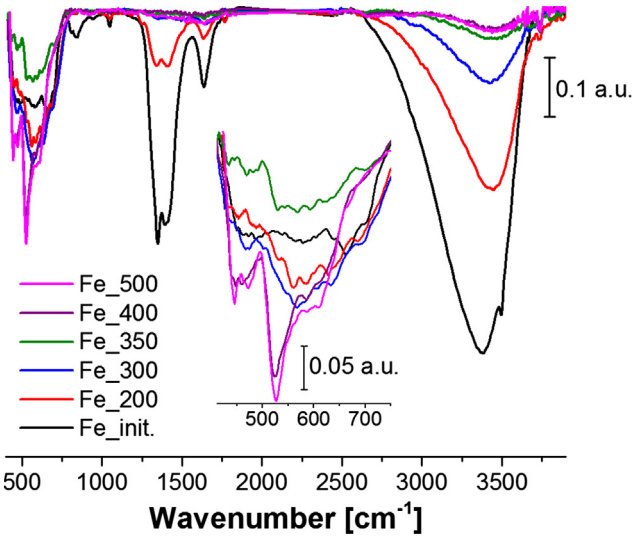

Fig. 3. ATR-FTIR spectra of the samples.

did not demonstrate other thermal transformations. This is possible in case it consisted of the phase that was stable in these circumstances: hematite.

According to the literature, the exothermic process at 460 °C (for Fe_200 and Fe_300) is γ → α conversion of Fe_2O_3 [18,19,15]. For the initial material, this peak was shifted to higher temperatures. For the Fe_400 sample, a small exothermic peak in the range of 420–560 °C can be distinguished at the enlarged scale. Taking into account the fact that the phase transition occurs over a wide temperature range (unlike melting, for example), it was concluded that the maghemite to hematite transition occurs but the amount of the phase being transited is low.

At 200–270 °C the transition magnetite → maghemite usually takes place. The exothermic peak in this region was observed for Fe_300 only. Also, this peak seemed to be shifted to 180 °C for the Fe_200 sample. So, it can be concluded that both these samples contained magnetite.

The Fe_init. sample showed much more complicated thermal behavior. Two endothermic processes (at ~110 and ~220 °C) cannot be explained by transitions in the Fe-O system. It was proposed, that the sample obtained by PLA in air contained nitrogen in any possible form (nitride, nitrite, etc.). Since the laser ablation is a high-energy intensive nonequilibrium process, nitrogen from air can be ionized and then can interact with iron and oxygen. So, these two peaks may belong to transformations of N-containing iron compounds (see, for example, DSC and DTA data for iron nitrides in [20]). Since the annealed samples did not exhibit these transformations, it was concluded that nitrogen leaves the sample at the heating. This is also proved by the TGA data (Fig. S1 in the Supplementary material) that exhibited the mass loss (up to 20%) of the sample during the temperature rising up to 250 °C.

Supplementary data associated with this article can be found, in the online version, at https://doi.org/10.1016/j.apsusc.2018.08.116.

Thus, DSC data indicated that the samples treated at 500 °C and higher temperatures may be represented by the hematite phase. The sample heated up to 400 °C showed the low-intense γ → α conversion of Fe_2O_3 only. The Fe_200 and Fe_300 samples contained magnetite that transformed to maghemite and hematite under heating. The powder obtained by PLA in air without thermal treatment presumably contained nitrogen-iron compounds, formed from air nitrogen under laser radiation.

3.3. Spectroscopic study of the materials

Fig. 3 shows the ATR-FTIR spectrum in the range of 400–4000 cm^{-1} and Inset shows the range of 400–750 cm^{-1}. The broad band at 3400–3500 cm^{-1} belonging to H—OH stretching [21] decreases with the increasing temperature of the samples' treatment. The samples Fe_init. and Fe_200 exhibited bands at 1350 and 1045 cm^{-1}, which belong to H_2O as well. These bands disappeared for the rest of the samples. Thus, the calcination affects the water absorption by the samples.

The presence of a number of intense bands in the region of 1200–1700 cm^{-1} most likely belongs to the vibrations of nitrogen-containing groups [22], which aligns with the DSC data (Section 3.2). The valence symmetric and asymmetric vibrations of NO_2 (1260–1390 cm^{-1} and 1490–1660 cm^{-1}) groups and valence N=O oscillations of monomers (1450–1680 cm^{-1}) and dimers (1250–1420 cm^{-1}) were found, as well as deformation vibrations of the NH and NH_2 types that, in addition to the bands at 1550–1650 cm^{-1}, exhibit bands at 700–850 cm^{-1}. The same vibration groups associated with the nitrogen atom are characteristic to nitrogen-containing iron compounds. For example, in the case of nitrates $Fe(NO_3)_3 \cdot 9H_2O$, oscillations are observed at 835, 1361, 1615, 1785 and 3230 cm^{-1} [22]. In [23], the IR bands at 3382, 3282 and 1610 cm^{-1} for the Fe/fumed SiO_2 sample were attributed to the asymmetric stretch, the symmetric stretch and the asymmetric deformation of an amide species NH_2 adsorbed on Fe sites, respectively. Annealing led to a sharp decrease in the intensity of the bands associated with the nitrogen, and for samples annealed at a temperature of 300 °C or higher, they no longer appear.

Concerning iron oxides, all the spectra showed bands in the region of 700–430 cm^{-1} belonging to iron–oxygen stretching vibration [24,25]. Bands at 580–590 cm^{-1} and 430–440 cm^{-1} correspond to the intrinsic stretching of the tetrahedral and octahedral sites of the inverse spinel cubic of Fe_3O_4 [15]. However, it seems to be impossible to distinguish between different iron oxides using these spectra.

Raman spectra of the NPs obtained are presented in Fig. 4. The initial sample is shown to contain magnetite only [9]. Characteristic broad bands of magnetite around 670, 310 and 540 cm^{-1} are clearly seen. According to Shebanova and Lazor, these bands are assigned for a magnetite crystal: 668(a_{1g}), 538 (T_{2a}) and 306(e_g) [26]. It should be noted that the Raman spectroscopic study of the powders obtained was complicated, since the very low radiation intensities must be used to avoid the transition of magnetite to hematite as a result of the local heating. This kind of transition is known [15,26,27]. That is why the sensitivity may be was too low to distinguish the small amount of nitrogen-containing species in the spectrum.

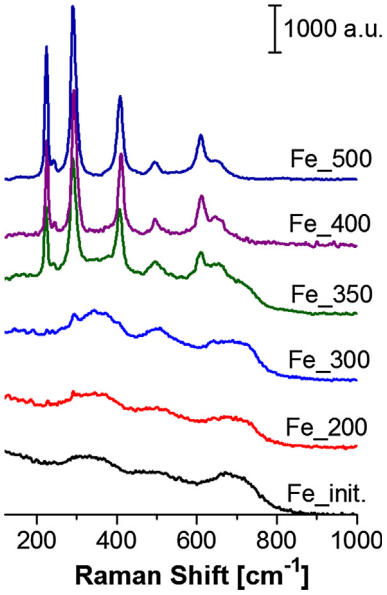

Fig. 4. Raman spectra of the samples.

Thermal treatment of the initial sample at 200 °C did not lead to Raman spectra change. However, 300 °C heating resulted in narrowing and a slight shift of the bands, even though the resulting spectrum cannot be analyzed uniquely. That is why the sample with the thermal treatment at 350 °C was prepared. Its Raman spectrum showed maghemite (651 (a_{1g}), 508 (T_{2g}), 360 (e_g) cm^{-1}) and hematite (605 (e_g), 491 (a_{1g}), 401 (e_g), 285 (e_g), 240 (e_g), 220 (a_{1g}) cm^{-1}) band appearance [27,28]. The subsequent thermal treatment led to the increasing of α- and γ-Fe_2O_3 content and resulted in pure hematite signals after heating the sample at 500 °C.

Thus, Raman data did not exhibit nitrogen presence in the samples, but it allowed one to distinguish between the iron oxides phases. The initial nanopowder obtained by PLA in air consisted of magnetite. Thermal treatment of the sample at 350 °C led to the formation of the mixture of magnetite, maghemite and hematite (the transformation started at 300 °C). Heating at 400 °C resulted in the decrease of magnetite and an increase of hematite, while 500 °C calcined material contained hematite only.

3.4. Microscopic study of the materials

Fig. 5 represents the TEM images of the initial powder obtained by Fe target ablation in air. The sample contains three different structural

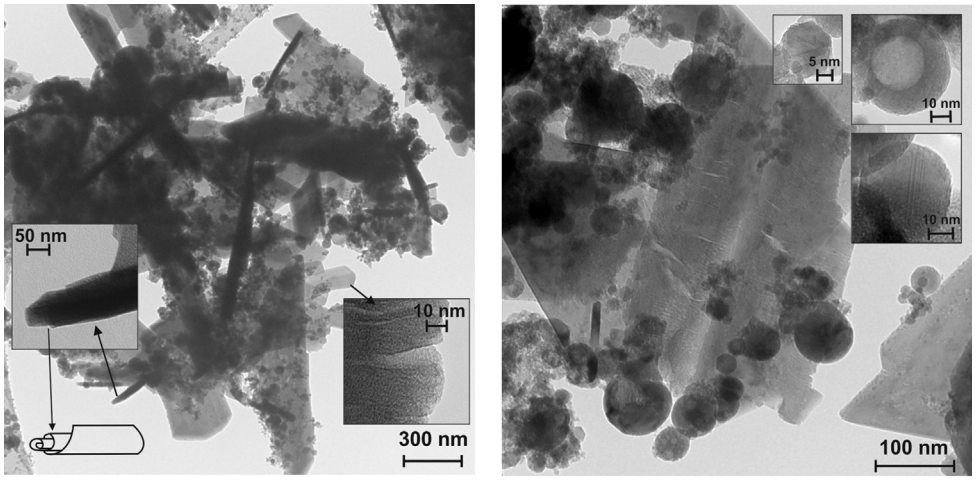

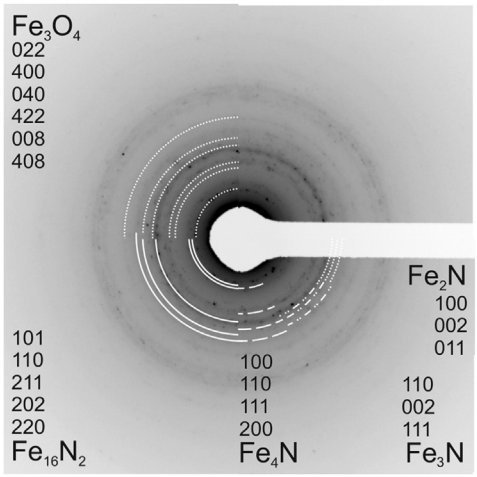

Fig. 5. TEM (a, b) and SAED (c) for Fe_init. sample. SAED analysis in (c): upper right quarter–dot line for Fe_3O_4 (#04-018-0091); lower right quarter–solid line for $Fe_{16}N_2$ (#01-070-6150); lower left quarter–dash line for Fe_4N (#01-083-0875), dash-dot-dot line for Fe_3N (#04-007-3379), dot line for Fe_2N (#01-072-2126).

elements. Most of the powder is presented by the 2–D lamellar structures. These lamellas can achieve 1 μm in length and width at the thickness of below 10 nm. The microstructure of these lamellas can be seen in the inset in Fig. 5a: a homogenous “fabric” with flexures and wrinkles. The next structural element of the sample is twisted lamellas (see inset in Fig. 5a). The twisted lamellas are spindle shaped. Their width is up to 150 nm, and their length may achieve 1 μm (just like the lamellas themselves). The third characteristic structure presented in the sample Fe_init. is the NPs (Fig. 5a, b). The NPs are mostly spherical; their size is in the range of 2–120 nm. Particles size distribution shows a maximum at 12–15 nm (Fig. S2 in the Supplementary material). Some NPs are hollow (right corner inset in Fig. 5b), since they exhibit less contrast in the center of the particles. The rest of the NPs are monocrystalline particles that may be covered with a thin shell (see other insets in Fig. 5b).

As was noted above, there are very few studies published on the production of iron-based nanopowders by laser ablation in the gaseous phase. The experimental conditions in the works published differ from those used in this work. Thus, the particles obtained differ in structure and size. Ablation using Nd-YAG laser but with much longer millisecond pulses and radiation power density of up to 10 MW/cm^2 in an atmosphere of the nitrogen and oxygen mixture led to the formation of only hematite nanoparticles [9]. The change in the gas mixture composition (the pressure; N_2/O_2 ratio) and the power density of the radiation affected only the dimensional characteristics of the particles (size up to 30 nm). The mechanisms of the particle formation under such conditions are fundamentally different from the one taking place at nanosecond pulsed ablation used in this work.

Nanoparticles of Fe_2O_3 were also obtained in [8], where ablation was carried out by ultraviolet radiation (308 nm) with an excimer XeCl laser (the pulse duration of 28 ns and the radiation power density of 120 MW/cm^2). The authors chosen conditions for the maximum oxidation of iron: the synthesis was carried out in a flow reactor (one liter per minute) in an oxygen medium. The gas medium and high-energy UV radiation contributed to the complete oxidation of iron to hematite. The average particle size for nanosecond ablation was much smaller (8 nm) than for long pulses described in [9], which closer to the results presented in this work.

The SAED data have shown (Fig. 5c and Table S1 in Supplementary material) that apart from the magnetite phase (Card #04-018-0091), iron nitrides may present in the sample: all the four marked in the figure or some of them. This correlates with the DSC data (see Section 3.2) and spectral analysis data (Section 3.3). Nitrogen presence was also proved by EDX analysis (Fig. 6). The calculated atomic content of N in the Fe_init. sample was 5.8 ± 0.6 at% and 1.5 ± 0.5 at% for the Fe_500 sample. Thus, nitrogen concentration decreased after thermal treatment, and about 1.5% may be presented by the adsorbed species that were detected by FTIR (see Section 3.3). Presumably, iron nitrides were formed via the interaction of iron and nitrogen from the air in a gas–plasma cloud during the ablation process.

To prove or disprove the hypothesis of the iron nitride formation, an experiment with the ablation of the Fe target in an Ar/O_2 atmosphere was carried out. As can be seen from the TEM image (Fig. 7), the sample Fe_Ar O_2 consists of only spherical NPs with the size in the range of 4–120 nm and the maximum at 15–18 nm (Fig. S3). According to the SAED data, only one phase was present in the sample–the magnetite (Card#00-019-0629, Table S2). Thus, in the absence of nitrogen, only magnetite phase was formed. Moreover, this phase is of the 227 space group with a cubic syngony, which has higher symmetry than the monoclinic one (for the sample Fe_init.). Therefore, N_2 presence during the ablation not only led to the formation of iron nitrides but affected the magnetite crystallization process, resulting in the growth of the less symmetrical phase.

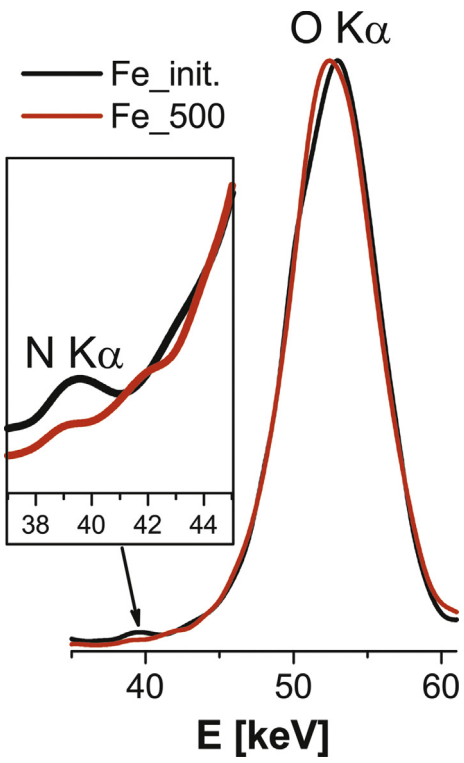

Fig. 6. Fragment of the EDX spectra for Fe_init. and Fe_500 samples.

However, thermal treatment of Fe_init. at 200 °C resulted in formation of the magnetite 227 space group as well (Card#00-019-0629). The SAED data are presented in Fig. 8c and in Table S3. The sample lost nitrogen completely after heating. Thus, the temperature treatment led to the oxidation of iron nitrides and magnetite recrystallization.

Concerning the microstructure, in the Fe_200 sample the 2–D lamellas are still present (Fig. 8a). But they show a more faceted structure with larger structural elements and higher regularity. They consist of a net-like continuous structure made of elements about 2–5 nm in size. The flexure and wrinkle characteristics of the initial sample disappear here. Twisted lamellas can still be found in the sample. They transformed into the denser rolls. Apparently, all these structural changes are the result of the recrystallization during nitrogen loss and the oxidation of the iron-containing sample during heating. Spherical NPs' size distribution in the Fe_200 sample widened to 5–195 nm with the maximum position still at 12–15 nm (Fig. 8b and Fig. S4). The share of large particles did not increase, but their size increased. So, thermal treatment did not affect particle size much.

Further heating to 300 °C led to a greater loosening of the structure of lamellas and rolls (Fig. 9a). Monocrystalline particles were still present (Fig. 9b), but their phase composition changed. The SAED data show that magnetite partly transformed to maghemite and hematite (Fig. 9c, Table S4). In addition to that, the particles' size increased: the distribution occupied the region of 4–230 nm, and the maximum was 20 nm (Fig. S5).

Fig. 10 shows the TEM images of powder calcined at 400 °C. Particle enlargement due to their concretion and recrystallization can be observed. The larger particles seem to blur their boundaries and transform into a joint 3–D structure. Separate particle size was measured; it was in the region of 8–170 nm. The lower limit increased, but the higher limit decreased compared with the Fe_300 sample. This can be explained by the fact that larger particles cannot be distinguished in an almost

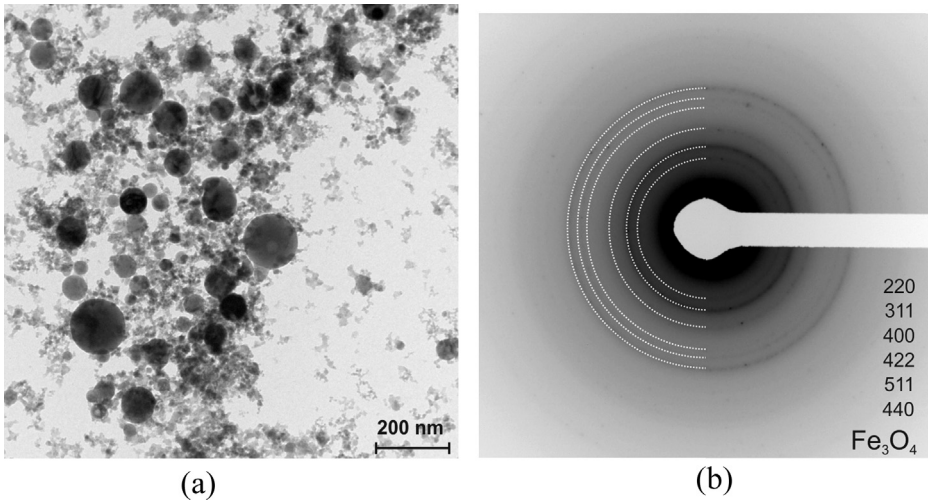

Fig. 7. TEM (a) and SAED (b) for Fe_Ar O_2 sample.

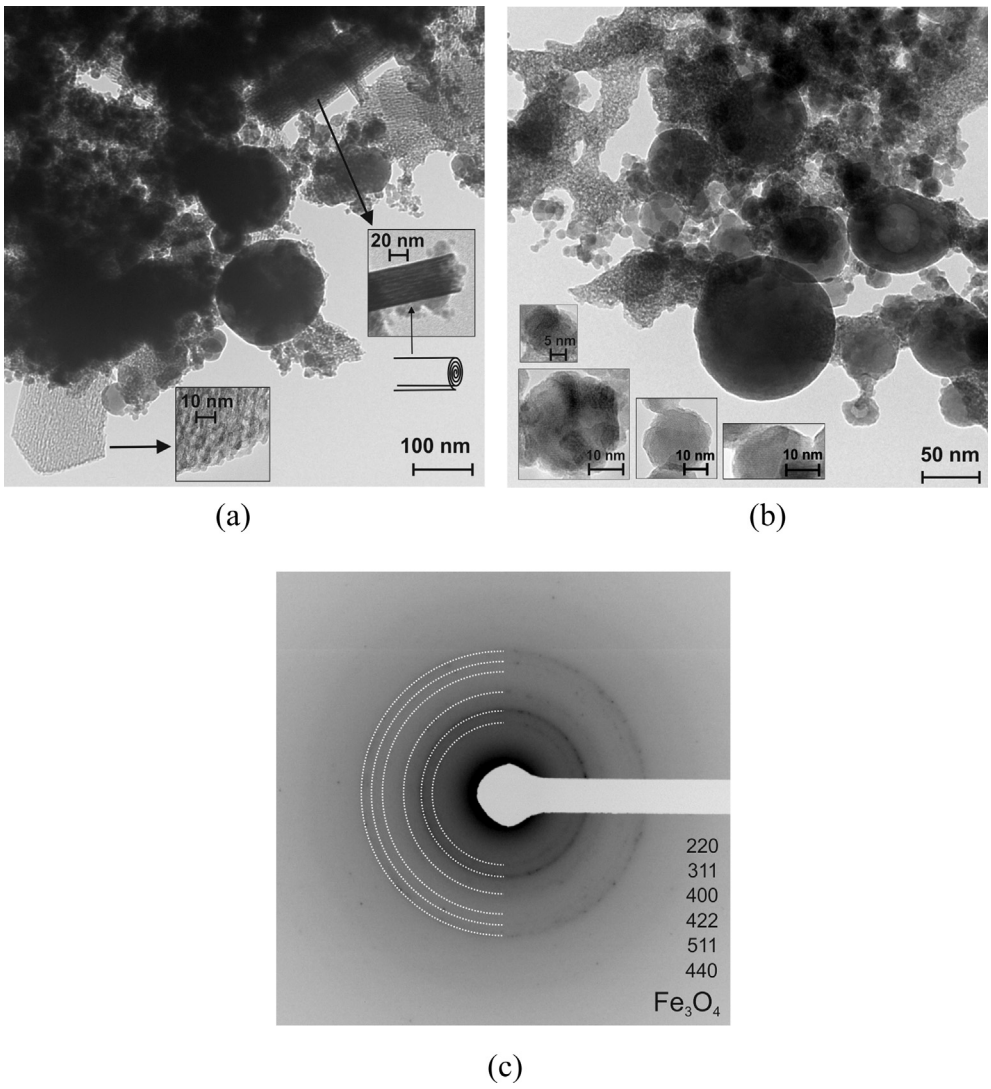

Fig. 8. TEM (a, b) and SAED (c) for Fe_200 sample.

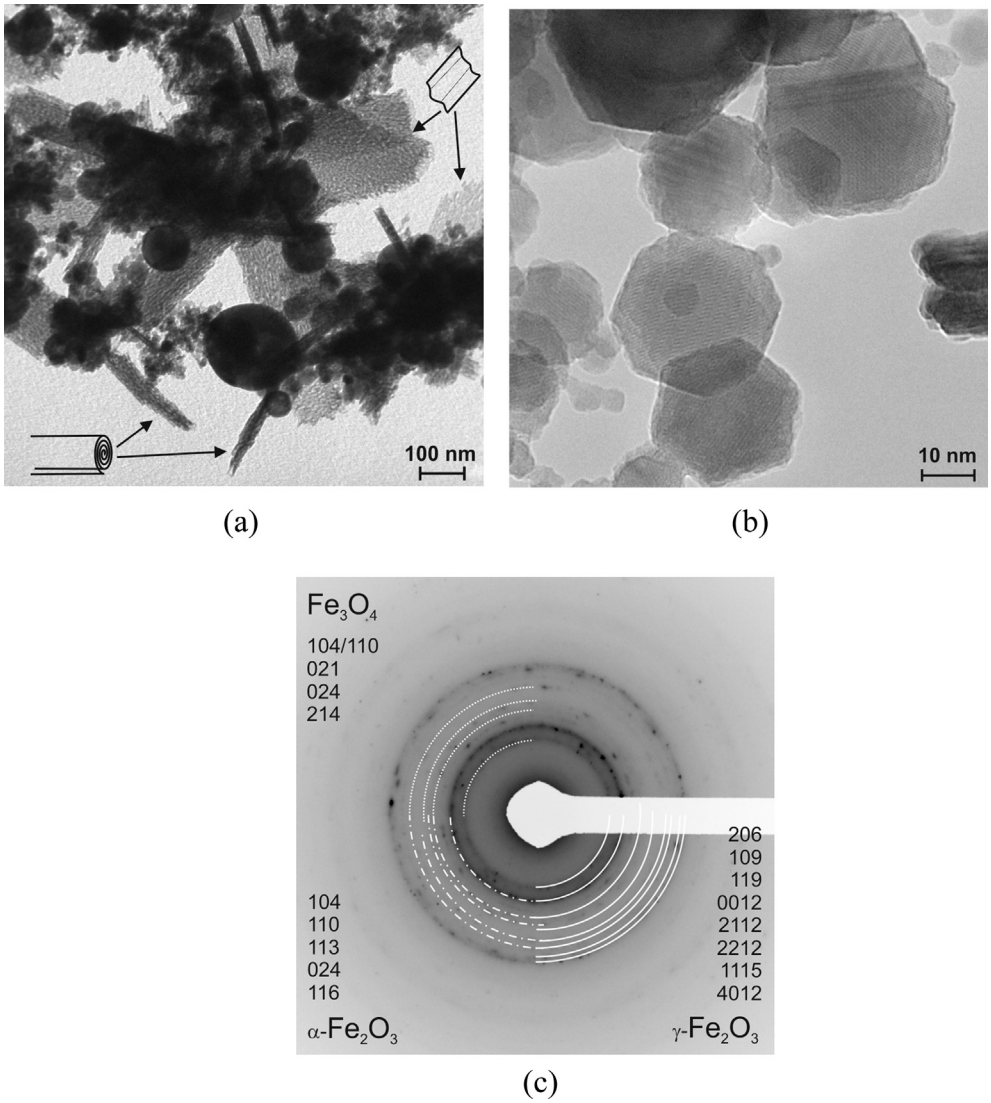

Fig. 9. TEM (a, b) and SAED (c) for Fe_300 sample. SAED analysis in (c): upper right quarter–dot line for Fe_3O_4 (#04-012-7038); lower right quarter–dash-dot line for α-Fe_2O_3 (#00-001-1053); lower left quarter–solid line for γ-Fe_2O_3 (#04-016-4345).

monolithic 3–D structure. Particles size distribution maximum was at 30–35 nm (Fig. S6), which is larger than for the samples calcined at 200 and 300 °C. The SAED data analysis results showed the presence of magnetite, maghemite and hematite in the sample (Fig. 10c, Table S5). However, it is assumed that the main product in this sample is hematite, since it did not show significant thermal transformations on the DSC curve (see Section 3.2).

The TEM images of the Fe_500 sample are presented in Fig. 11. The particles lost their individual boundaries. It is impossible to estimate the particles' size in this sample. The 3–D net-like structure formed consists of hematite only (Fig. 11c and Table S6). Thus, thermal-assisted complete phase transformation occurred at 500 °C.

It is interesting to notice that pores in the particles form in the Fe_400 and Fe_500 samples while a 3–D net-like structure appears (light circle spots in Figs. 10b and 11b). Apparently, recrystallization may affect the specific surface area of the sample in two ways. Either it may decrease the S_{BET} that is anticipated, since the particles size increased, or it can increase the S_{BET}, since more pores are formed. To find out what is more likely, S_{BET} of the samples was measured. The BET data are presented in Table 1.

For the initial sample, two values of S_{BET} are presented. The first one (100.1 cm^2) was obtained when the sample degassing was carried out at 200 °C for 2 h (the standard procedure that was used for the rest of the samples). But, as it shown above, thermal treatment at this temperature affects both the structure and the composition of the sample; that is, Fe_init. can be partly transformed into Fe_200. The S_{BET} values for these two samples are rather close (100.1 and 100.8 cm^2). That is why BET measurements at room temperature degassing were carried out for the Fe_init. sample. The resulting S_{BET} value was quite unexpected: 17.7 cm^2. Thus, the specific surface area of the initial sample was much lower than that of Fe_200.

So, the S_{BET} value increased five times, and the porosity increased three times for the Fe_init. sample after heating at 200 °C. The possible explanation is structural changes in the sample during heating. Fe_init. contains lamellas with very smooth structures (see Fig. 5a and b). After a 200 °C treatment, the lamellas structures became looser and more faceted. They seem to be composed of separate but joint particles or structural elements of 2–5 nm. These structural transformations can

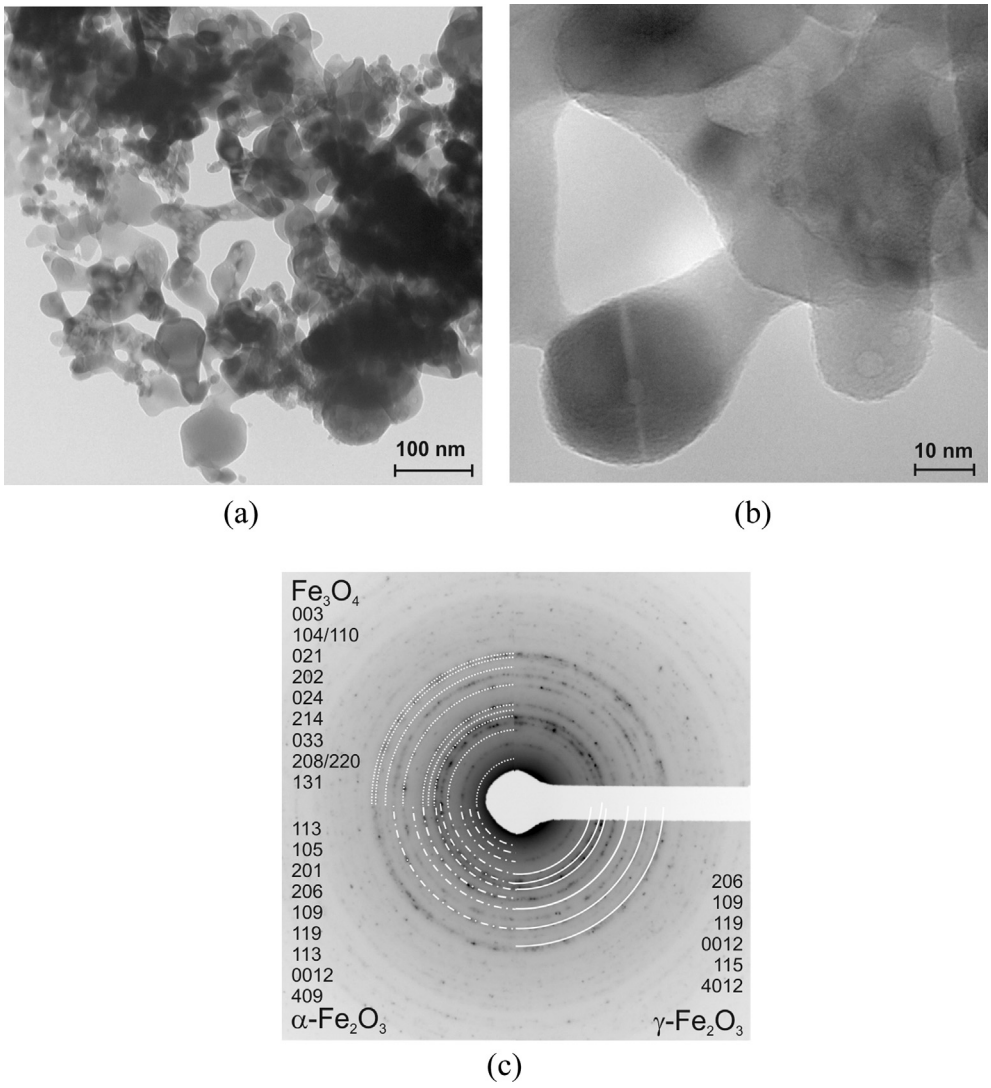

Fig. 10. TEM (a, b) and SAED (c) for Fe_400 sample. SAED analysis in (c): upper right quarter–dot line for Fe_3O_4 (#04-012-7038); lower right quarter–dash-dot line for α-Fe_2O_3 (#04-007-2140); lower left quarter–solid line for γ-Fe_2O_3 (#04-016-4345).

increase the S_{BET} value and porosity.

The subsequent decrease of S_{BET} from 100.8 cm^2 for Fe_200 to 19.2 cm^2 for Fe_500 is the result of particle enlargement and the joint 3–D structure formation. The porosity value reaches the maximum for the Fe_300 sample and further decreases (Table 1). This maximum can be explained by the structural transformations as well. Lamellas in Fe_300 are looser and more porous than in Fe_200, and the porosity increases. But in the Fe_400 sample, the lamellas disappeared completely, forming a 3–D joint structure, and porosity decreased. Pore average diameter showed a minimum in the Fe_200 sample and continued rising (Table 1). Presumably, the minimum is also connected with the lamellas restructuring after 200 °C of heating.

Thus, the microstructure of the powder obtained via PLA in air and its phase composition are changed with the thermal treatment. The original sample contained lamellar structures (including twisted ones) and spherical monocrystalline particles. These structures became faceted and restructured with the rising temperature, and an almost monolithic 3–D structure was formed after 400–500 °C of heating. The Fe_init. sample contained iron–nitrogen compounds, which oxidized to pure magnetite after 200 °C of heating. The Fe_300 and Fe_400 samples are presented by a mixture of magnetite, maghemite and hematite phases. Thermal treatment at 500 °C led to complete oxidation with the hematite-only formation.

3.5. Magnetic properties study of the materials

The magnetization curves for the powders obtained by PLA in air and the subsequent thermal treatment are presented in Fig. 12. All the curves exhibit hysteresis loops characteristic of ferromagnetic materials. Saturation of the magnetization was not observed for all the curves. Parameters obtained from the VSM data are summarized in Table 2 (M_s was determined by extrapolating the magnetization curve to the *y* axis). The coercivity increases as the heat temperature increases. This may be connected with the phase composition change: in this series, the proportion of hematite content increases. As shown in [29], thermal treatment of magnetite may lead to such a result. Also, coercivity is a structure-sensitive characteristic. The larger particles and 3–D continuous net-like structure in the Fe_500 sample provides a

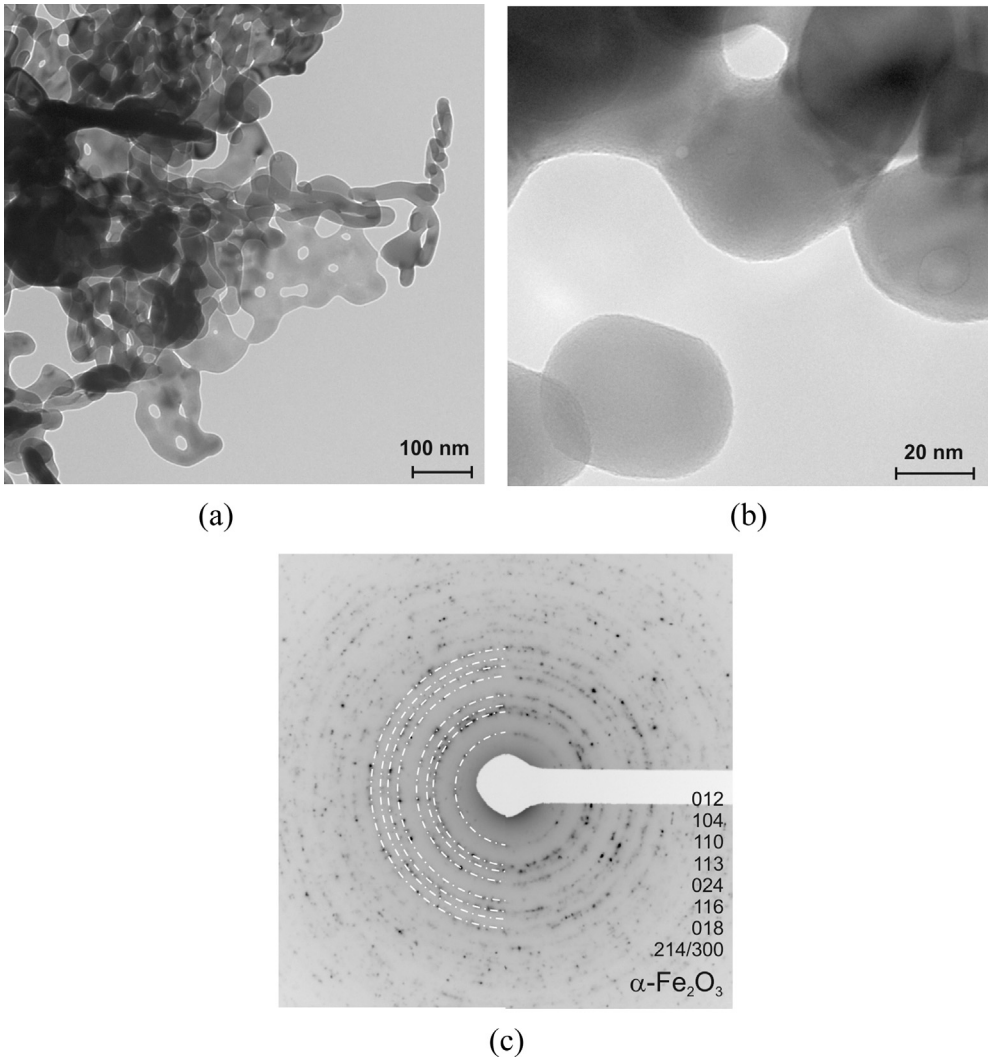

Fig. 11. TEM (a, b) and SAED (c) for Fe_500 sample.

Table 1
BET data for the samples.

Sample	S_{BET} [cm^2]	Pore volume [cm^3/g]	Pore average diameter [nm]
Fe_init.	100.1/17.7[a]	0.038	8.5
Fe_200	100.8	0.114	4.5
Fe_300	67.2	0.155	9.2
Fe_400	28.5	0.102	11.5
Fe_500	19.2	0.056	11.6

[a] The value obtained for the sample degassed in a vacuum (10^{-2} Torr) at room temperature for 4 h. All the rest data in this row belong to the degassing at 200 °C for 2 h.

larger field value for material demagnetization. Krajewski et al. [29] explained this with the fact that larger particles formed as a result of sintering containing more defects, dislocations and strains. This affects magnetic properties, and the coercivity rises.

The H_C rising is accompanied by the M_s decrease from the Fe_200 to the Fe_500 samples. The Fe_init. sample, which has the lowest H_C, showed an M_s lower than that for Fe_200, almost equal to that for Fe_300, and larger than for the rest of the samples. This may be explained by the presence in the Fe_init. sample of nitrogen-containing iron compounds, the magnetic properties of which differ from those for iron oxides. So, the highest magnetization saturation was shown by the sample heated to 200 °C. As it previously shown, this sample contained

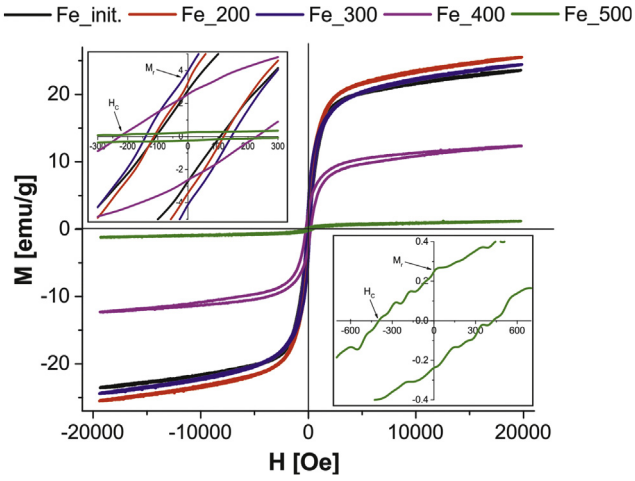

Fig. 12. VSM data for the samples.

only magnetite with the cubic syngony. With the phase composition change (maghemite and hematite appearance), M_s decreases. Remanent magnetization showed a maximum value for the sample heated to 300 °C. Thus, this material may have the optimal phase composition and structure for using it in processes that require NPs with the

Table 2
Parameters obtained from VSM data: H_C – coercivity; M_s – saturation magnetization; M_r – remanent magnetization.

Sample	H_C [Oe]	M_s [emu/g]	M_r [emu/g]
Fe_init.	108	19.3	2.79
Fe_200	116	20.8	3.36
Fe_300	142	19.4	4.03
Fe_400	228	10.1	2.59
Fe_500	413	0.7	0.24

Table 3
Zeta-potential measurement results for the samples (m = 20 mg/l).

Sample	pH	Zeta-potential [mV]
Fe_init.	4.25	+44.3
Fe_200	4.72	+26.3
Fe_300	5.30	+27.3
Fe_400	6.30	**−21.9**
Fe_500	5.30	+29.0

permanent magnetic properties. Thus, the materials obtained exhibit quite different magnetic parameters and can be used for different purposes in biomedicine and other fields.

3.6. Zeta-potential study of the materials

A possible application of the obtained materials in the field of biomedicine requires them to allow the obtainment of stable dispersions in water and water solutions (saline solution, for example). To estimate the stability of NPs' dispersions, zeta-potential (ζ) measurements were carried out. The results are presented in Table 3. The Fe_init. sample has the highest positive potential and can form the most stable dispersions in water. The samples annealed at 200, 300 and 500 °C exhibit a ζ value between +26 and +29 mV. The positive trend (from the Fe_200 to Fe_500 samples) may be noticed, but the Fe_400 sample shows an unexpected ζ value. In addition to the higher pH of the dispersion obtained after Fe_400 sonication in water, the negative ζ was found. Thus, the stability of the dispersion may be close to that of other annealed samples, but the surface state of the Fe_400 NPs differs dramatically. Presumably, structural and phase transformations that occur starting from 400 °C led to the surface state changes. Remembering the TEM data, at this stage the lamellas disappear, and in addition to the NPs, they start the formation of a joint 3–D structure. That is why, hypothetically, this sample may contain the largest number of defects, dislocations and strains, which formed as a result of first sintering stage. Further heating may lead to a partial defect recovery, changing surficial properties of the sample.

This is an important point, since different biomedical applications require not only dispersions stability but also different surface states of the NPs, allowing them to bind with required molecules, for example.

4. Conclusion

A number of magnetic NPs with varying characteristics were obtained as a result of synthesis via nanosecond PLA of the iron target in air and the subsequent annealing treatment.

The powder initially obtained by PLA contains spherical NPs of iron oxide with the magnetite (Fe_3O_4) monoclinic structure with an admixture of lamellas and rolls, presumably represented by iron nitrides. The concentration of nitride compounds in the samples is supposed to be small, which makes it impossible to find them on XRD patterns. But they were detected by highly-localized SEAD method. Indeed, it is not easy to prove whether iron nitrides were formed or nitrogen-containing molecules were adsorbed onto the surface. Most likely, both variants coexist at the same time that is confirmed by the SAED, XRD, DSC/TGA, EDX, and FTIR data. The particles obtained are characterized by high sedimentation stability in aqueous colloids and ferromagnetic behavior at room temperature with a sufficiently high residual magnetization. Thus, the initial sample may be of interest for use in the form of an aqueous colloidal solution in biomedicine.

Annealing led to the removal of nitrides from the sample, the enlargement of the particles and the increase of the remanent magnetization. The Fe_200 sample was composed of pure magnetite and exhibited the highest specific surface area. It can be used in any application where a pure magnetite phase is required. The sample annealed at 300 °C has an optimal phase composition and structure for its use in processes that require NPs with permanent magnetic properties. For example, it can be used as an active component of magnetic fluids used for controlling mechanical (viscosity) and optical (transmission of electromagnetic radiation in a wide range, especially in IR and THz) properties. Despite the decrease in the zeta potential, the water colloid of these particles is still sufficiently stable, which also allows their use in biomedicine for hyperthermia, drug delivery and so on.

A further increase in the annealing temperature led to a considerable rearrangement, restructure and change of other particles' characteristics. A sharp change in the surface state of the Fe_400 sample, which was revealed in the ζ opposite sign appearing, requires further study of the samples surface states and the effect of the solution's pH. The decrease in the magnetic characteristics (in particular, the decrease in the saturation magnetization) after annealing at 500 °C is associated with the formation of a pure hematite phase with the concomitant sintering and enlargement of the NPs. Along with that, phase-mixed (as Fe_400 contained magnetite, maghemite and hematite) and pure hematite NPs are promising materials for catalysis, such as cracking of petroleum.

Acknowledgements

This study was supported by Russian Science Foundation (RSF), Project # 18-19-00268.

References

[1] H. Zeng, X.W. Du, S.C. Singh, S.A. Kulinich, S. Yang, J. He, W. Cai, Nanomaterials via laser ablation/irradiation in liquid: a review, Adv. Funct. Mater. 22 (2012) 1333–1353.
[2] D. Zhang, B. Gökce, S. Barcikowski, Laser synthesis and processing of colloids: fundamentals and applications, Chem. Rev. 117 (2017) 3990–4103.
[3] M. Dell'Aglio, R. Gaudiuso, O. De Pascale, A. De Giacomo, Mechanisms and processes of pulsed laser ablation in liquids during nanoparticle production, Appl. Surf. Sci. 348 (2015) 4–9.
Shih et al., 2018 C.Y. Shih, R. Streubel, J. Heberle, A. Letzel, M.V. Shugaev, C. Wu, M. Schmidt, B. Gökce, S. Barcikowski, L.V. Zhigilei, Two mechanisms of nanoparticle generation in picosecond laser ablation in liquids: the origin of the bimodal size distribution, Nanoscale 10 (2018) 6900–6910.
[5] T. Sasaki, Y. Shimizu, N. Koshizaki, Preparation of metal oxide-based nanomaterials using nanosecond pulsed laser ablation in liquids, J. Photochem. Photobiol. A. 182 (2006) 335–341.
[6] V. Svetlichnyi, A. Shabalina, I. Lapin, D. Goncharova, Metal oxide nanoparticle preparation by pulsed laser ablation of metallic targets in liquid, in: D. Yang (Ed.), Applications of Laser Ablation – Thin Film Deposition, Nanomaterial Synthesis and Surface Modification, InTech, Croatia, 2016, pp. 245–263.
[7] E.M. Slavinskaya, A.I. Stadnichenko, V.V. Muravyov, T.Yu. Kardash, E.A. Derevyannikova, V.I. Zaikovskii, O.A. Stonkus, I.N. Lapin, V.A. Svetlichnyi, A.I. Boronin, Transformation of Pt-CeO2 mechanical mixture of pulsed laser-ablated nanoparticles to highly active catalyst for CO oxidation, ChemCatChem. 10 (2018) 2232–2247.
[8] M. Ullmann, S.K. Friedlander, A. Schmidt-Ott, Nanoparticle formation by laser ablation, J. Nanoparticle Res. 4 (2002) 499–509.
[9] Z. Wang, Y. Liu, X. Zeng, One-step synthesis of γ-Fe_2O_3 nanoparticles by laser ablation, Powder Technol. 161 (2006) 65–68.
[10] M.G. Adimoolam, N. Amreddy, M. Rao Nalam, M.V. Sunkara, A simple approach to design chitosan functionalized Fe3O4 nanoparticles for pH responsive delivery of doxorubicin for cancer therapy, J. Magn. Magn. Mater. 448 (2018) 199–207.
[11] S.I. El-Dek, M.A. Ali, S.M. El-Zanaty, S.E. Ahmed, Comparative investigations on ferrite nanocomposites for magnetic hyperthermia applications, J. Magn. Magn. Mater. 458 (2018) 147–155.
[12] X. Wang, M. Zhang, J. Zhao, G. Huang, H. Sun, Fe3O4@polyaniline yolk-shell micro/nanospheres as bifunctional materials for lithium storage and electromagnetic wave absorption, Appl. Surf. Sci. 427 (2018) 1054–1063.

[13] L.P. Wang, Y.B. Huang, Y.H. Lai, Surface enhanced Raman scattering activity of dual-functional Fe3O4/Au composites, Appl. Surf. Sci. 435 (2018) 290–296.
[14] A.J. Bruno, J.R. Correa, E. Pelaez-Abellan, E. Urones-Garrote, A novel method for the functionalization of aminoacids L-glycine, L-glutamic acid and L-arginine on maghemite/magnetite nanoparticles, J. Magn. Magn. Mater. 456 (2018) 87–91.
[15] V.A. Svetlichnyi, A.V. Shabalina, I.N. Lapin, D.A. Goncharova, D.A. Velikanov, A.E. Sokolov, Characterization and magnetic properties study for magnetite nanoparticles obtained by pulsed laser ablation in water, Appl. Phys. A 123 (2017) 763–771.
[16] C.C.P. Chan, H. Gallard, P. Majewski, Fabrication of amine-functionalized magnetite nanoparticles for water treatment processes, J. Nanopart. Res. 14 (2012) 828–839.
[17] D.A. Velikanov, RU Patent 2341810, 2008.
[18] D.L.A. De Faria, S. Venancio Silva, M.T. De Oliveira, Raman microspectroscopy of some iron oxides and oxyhydroxides, J. Raman Spectrosc. 28 (1997) 873–878.
[19] M. Aliahmad, N. Nasiri Moghaddam, Synthesis of maghemite (γ-Fe_2O_3) nanoparticles by thermal-decomposition of magnetite (Fe_3O_4) nanoparticles, Mater. Sci. Poland 31 (2013) 264–268.
[20] M. Widenmeyer, T.C. Hansen, R. Niewa, Formation and decomposition of metastable α-$Fe_{16}N_2$ from in situ powder neutron diffraction and thermal analysis, Z. Anorg. Allg. Chem. 639 (2013) 2851–2859.
[21] F. Fajaroh, H. Setyawan, W. Widiyastuti, S. Winardi, Synthesis of magnetite nanoparticles by surfactant-free electrochemical method in an aqueous system, Adv. Powder Technol. 23 (2012) 328–333.
[22] F.A. Miller, C.H. Wilkins, Infrared spectra and characteristic frequencies of inorganic ions. their use in qualitative analysis, Anal. Chem. 24 (1952) 1253–1294.
[23] L. Wang, Q. Xin, Y. Zhao, G. Zhang, J. Dong, W. Gong, H. Guo, In situ FT-IR studies on catalytic nature of iron nitride: identification of the N active site, ChemCatChem 4 (2012) 624–627.
[24] B.K. Pandey, A.K. Shahi, J. Shah, R.K. Kotnala, R. Gopal, Optical and magnetic properties of Fe2O3 nanoparticles synthesized by laser ablation/fragmentation technique in different liquid media, Appl. Surf. Sci. 289 (2014) 462–471.
[25] R.A. Ismail, G.M. Sulaiman, S.A. Abdulrahman, T.R. Marzoog, Antibacterial activity of magnetic iron oxide nanoparticles synthesized by laser ablation in liquid, Mater. Sci. Eng., C 53 (2015) 286–297.
[26] O.N. Shebanova, P. Lazor, Raman spectroscopic study of magnetite ($FeFe_2O_4$): A new assignment for the vibrational spectrum, J. Solid State Chem. 174 (2003) 424–430.
[27] O.N. Shebanova, P. Lazor, Raman study of magnetite (Fe_3O_4): Laser-induced thermal effects and oxidation, J. Raman Spectrosc. 34 (2003) 845–852.
[28] O.S. Ivanova, I.S. Edelman, R.D. Ivantsov, E.A. Petrakovskaja, D.A. Velikanov, N.N. Trofimova, Y.V. Zubavichus, Ensembles of γ-Fe_2O_3 nanoparticles formed during devitrification of borate glasses, Solid State Phenom. 215 (2014) 173–178.
[29] M. Krajewski, K. Brzozka, M. Tokarczyk, G. Kowalski, S. Lewinska, A. Slawska-Waniewska, W.S. Lin, H.M. Lin, Impact of thermal oxidation on chemical composition and magnetic properties of iron nanoparticles, J. Magn. Magn. Mater. 458 (2018) 346–354.